CHAPTER 5: S doped Ag_2O photocatalysts

5.1 Introduction

Photocatalysis is a green and economical process that can resolve the current energy and environmental issues (Melchionna & Fornasiero, 2020; Molinari et al., 2020; J. Yu et al., 2012). This technique suffers from two significant issues. One is the rapid recombination of photo-generated electrons and holes pair after photo-excitation of the photocatalyst, resulting in lesser photocatalytic activity of the semiconductor material. Effective charge separation and appropriate adsorption of the targeted redox species on the photocatalyst can reduce this recombination problem. The second requirement for an efficient photocatalyst is having suitable conduction band (CB) and valence band (VB) positions. CB and VB should be above and below the reduction and the oxidation couple, respectively. Photocatalysis research demands semiconductor nanostructures with appropriate band structures that ensure charge separation and strong redox driving forces (Jatav et al., 2021; S. Kumar et al., 2019; U. Kumar, Das Chakraborty, et al., 2022; U. Kumar, Kuntail, et al., 2022; Pal et al., 2022).

Introducing defects like vacancies or dopants in the parent semiconductor material can increase charge separation and alter the bandgap and adsorption properties. For instance, Hezam et al. synthesized oxygen vacancy (OV) enriched ceria (CeO_2) with better charge separation and enhanced photocatalytic activity (Hezam et al., 2020). OV-generated defect sites can trap the photo-induced excited species to improve the charge carrier separation. Surface defects are also adsorption sites for the desired reactant. Furthermore, OVs and (cation or anion) doping also modify the electronic band structure of the parent semiconductor (Gleditzsch et al., 2019; Hirai et al., 2020; Mitra

et al., 2012; Serpone, 2006; Tang et al., 2018a). The dopant's orbitals may be introduced between the CB and VB or hybridized with pure analog orbitals (De et al., 2020; J. Zhao et al., 2020). Therefore, the semiconductor's bandgap can be widened or narrowed down depending on the nature of the defect.

Doping is also crucial in the context of the creation of OV defects (Chu et al., 2020; X. Li et al., 2018). The oxidation state of the dopant or its size can induce OVs. Doping by lower valent cations makes the semiconductor electron-deficient, and OVs are created to correct the resultant charge imbalance. For example, WO_3 (the oxidation state of W is +6) doped with Cr^{3+} resulted in OV formation for local charge compensation (F. Li et al., 2018). The adsorption behavior of the nanomaterials also changed due to such doping (K. V. Kumar et al., 2015; M. Liu, 2020; Zhong et al., 2013). High-pressure synthesis methods like solvothermal synthesis can also induce OV creation. Elevated pressure conditions balance the strains in the crystal lattice due to OV formation (Y. Huang et al., 2019; T. Liu et al., 2015; Jiaqi Zhang & Li, 2022). The lattice distortion strains due to substitution by larger anions can also cause OV formation (Gomez et al., 2020).

The visible range constitutes a significant portion of the solar spectrum. Small and moderate bandgap visible-light photocatalysts can efficiently use this visible range radiation. Ag_2O is a narrow bandgap semiconductor (1.2 - 1.5 eV) that can use a large part of the UV-visible spectrum. But the small bandgap also means that its VB or CB position may not be appropriate for the desired redox reaction. Pure Ag_2O photocatalysts also suffer from photo-stability and recombination issues (Gomez et al., 2020). Doping can widen this bandgap and give better charge separation for enhanced photocatalytic activity. For instance, Zn or Sr doped Ag_2O exhibits a wider bandgap (De et al., 2020; Kiani et al., 2019). As mentioned earlier, doping also modifies the

adsorption properties of the parent semiconductor, affecting the photocatalytic activity towards a target reactant. While density functional theory (DFT) calculations have predicted that oxygen vacancies will widen the Ag_2O bandgap, no validating experimental reports in literature correspond to this prediction. Hence, potentially Ag_2O with doping and vacancy defects could effectively be a new photocatalyst with better activity.

An extensive literature survey reveals very little photocatalysis research on developing such doped Ag_2O photocatalysts. Given the above perspective, the present study focuses on the change in structural and electronic properties of Ag_2O nanoparticles induced by sulfur (S) doping. Note that the structural and electronic properties of such S-doped Ag_2O have not been studied previously. Furthermore, S as a dopant can exhibit variable oxidation states (+6, +4, and -2); therefore, it is possible to generate charge imbalance in the Ag_2O system. Different sizes and charges of the dopant species can cause OV defects and change the electronic properties of the doped system.

Given the narrow bandgap of pure Ag_2O, the priority was to find whether S-doping could increase the material's bandgap. We conducted DFT calculations on several models with sulfur substituting oxygen or occupying an interstitial position with or without oxygen vacancies. The qualitative results indicated that sulfur substitution could widen the bandgap relative to the undoped one. Based on this prediction, experimental preparation of S-doped Ag_2O nanoparticles was conceived. The dopant mole percent was kept at a very low level ($\leq$1.25%) to prevent (S- based) the formation of compounds like Ag_2S, Ag_2SO_3, and Ag_2SO_4. A hydrothermal protocol was used to prepare pure and S-doped Ag_2O. X-ray diffraction (XRD) analysis demonstrated that S doping contracted the crystal lattice. X-ray photoelectron spectroscopy (XPS)

investigation detected oxygen vacancy formation in undoped and doped Ag_2O nanoparticles. The photoluminescence studies investigated the relative recombination efficiencies. The DFT calculation results combined with XRD and XPS analysis evidence led to the possible dopant position in the Ag_2O crystal lattice. Under visible light irradiation, the prepared S-doped Ag_2O nanoparticles exhibited enhanced photocatalytic activity towards RhB degradation. Experiments with scavenger molecules determined the active species responsible for photocatalytic activity. The collated information from various investigations led to the probable photocatalytic mechanism.

5.2 Experimental

5.2.1 Sample preparation

Synthesis of pure Ag_2O nanoparticles

Two millimoles (mmol) of $AgNO_3$ were dissolved in 40 ml DDDW water by continuous stirring for 15 minutes. Then, 0.2N NaOH was added dropwise into the previous solution. The addition of NaOH was continued until the pH of the reaction mixture reached 11. Then, the resulting mixture was transferred into a 100 ml stainless steel autoclave and heated in a hot-air oven at $180^{O}C$ for 24 hours. A black precipitate was formed. The precipitate was separated and washed several times with DDDW and ethanol. The end product was dried at $50^{O}C$ in a hot air oven to get the pure Ag_2O nanoparticles (denoted by B0).

Synthesis of sulfur-doped Ag_2O nanoparticles

Three different molar ratios of thiourea (CS $(NH_2)_2$) and $AgNO_3$ were used to synthesize three sulfur-doped Ag_2O (hereafter denoted by B1, B2, and B3) samples. The B1, B2, and B3 were prepared using 0.3, 1.25, and 2.5 mol% of thiourea. The first step

was to dissolve the desired amount of $AgNO_3$ in DDDW water and adjust the solution pH to 11. Then, the required amount of thiourea solution was added to this solution, maintaining the final solution pH at 11. The reaction mixture was stirred for another 15 minutes and transferred to a 100 ml stainless steel autoclave for hydrothermal treatment at $180^{O}C$ for 24 hours. Synthesized materials were washed with DDDW and ethanol. This step was followed by drying at $50^{0}C$ in a hot air oven to get the doped samples.

5.2.2 Computational details

All the theoretical calculations were performed using plane-wave DFT in the Vienna ab-initio simulation package (VASP). The models for all the investigations were created on the Medea-VASP platform. DFT calculations were carried out using generalized gradient approximation Perdew-Burke-Ernzerhoff (GGA-PBE) exchange-correlation functional and the projected augmented wave (PAW) pseudopotential. Initially, a 2x2x2 supercell was built from the Ag_2O unit cell (Card No: COD 4318188) and optimized using a 2x2x2 k-point mesh size and 520 eV plane-wave basis set energy cut-off. This perfect Ag_2O model is labeled as C0 in the rest of this article. Taking C0 as the base model, two types of sulfur doping possibilities were investigated. In one case, an oxygen atom in this perfect Ag_2O supercell model was substituted by a sulfur atom (CP1). The second model had the dopant sulfur atom placed in an interstitial site of the supercell (CP2).

Four more Ag_2O models with O-vacancy and S-doping defects were also designed and investigated. All calculations on these defect models were carried out with the optimized parameters used for the C0 model. The first defect model considered was the Ag_2O supercell with an O-vacancy (hereafter denoted by C1). In the second model, an S substituted an O in the C1 model (hereafter labeled as C2). This model, therefore, has an O-vacancy and oxygen substituted by sulfur. The third model (labeled as C3)

introduced the dopant S atom in an Ag_2O crystal interstitial position in the C1 prototype. Figure 5.1 shows the schematic of the C0, C1, and C2 models. Then, the S-doped formation energies of the respective systems were computed as per equations (5.1) and (5.2).

$$E_f(C2) = E_{defect}(C2) - [E_{C1} + \mu_S - \mu_O] \quad (5.1)$$

$$E_f(C3) = E_{defect}(C3) - [E_{C1} + \mu_S] \quad (5.2)$$

Here $E_f\ (C2)$ and $E_f\ (C3)$ represent the formation energies of C2 and C3 systems, respectively. The chemical potentials of S and O are denoted by μ_S and μ_O. The μ_O and μ_S were defined as energy per oxygen and sulfur atom from the O_2 (COD 2106877) and $(S_8)_4$ (COD 2002079) unit cells, respectively (X. Xiang et al., 2015). In addition, the density of states (DOS) of these models was collected from the optimized supercells by single point calculation using 8 × 8 × 8 K mesh and 400 eV energy cut-off value.

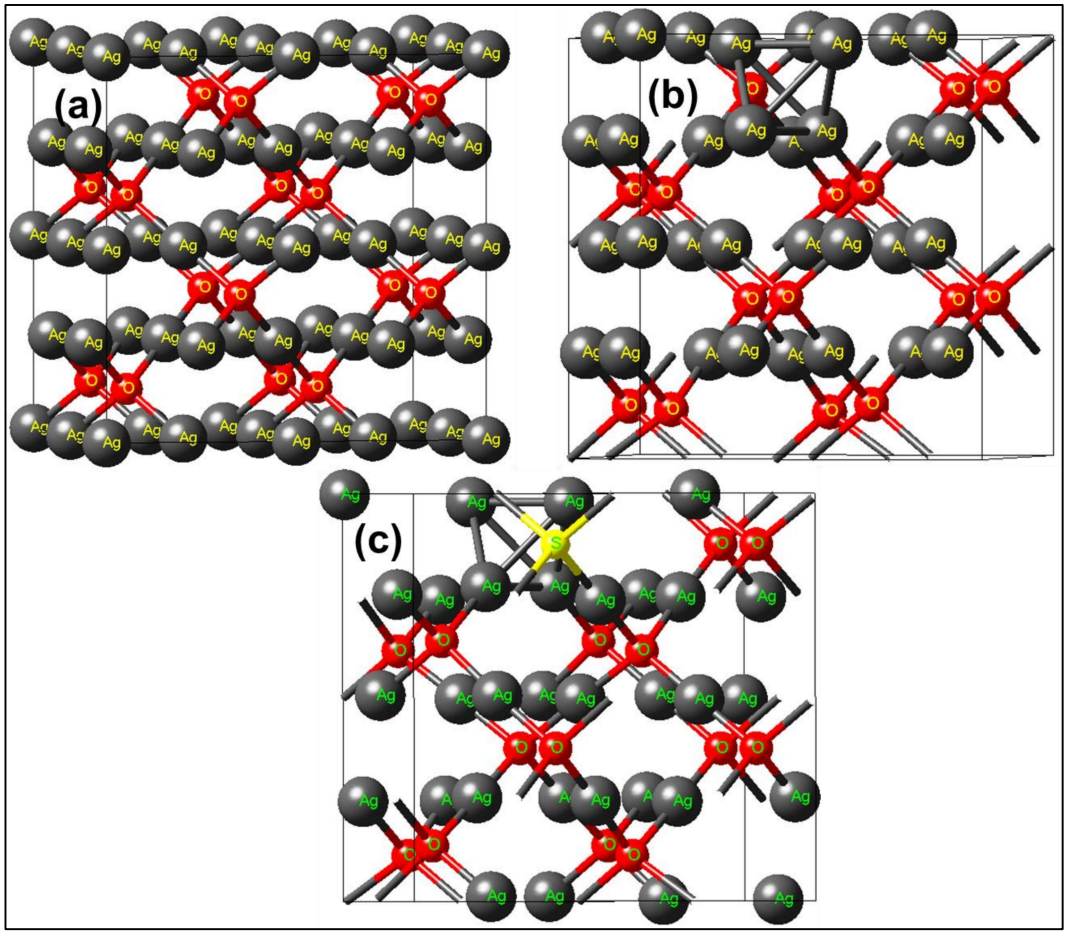

Figure 5.1 Optimized geometry of C0, C1, and C2 models.

5.2.3 Photocatalysis experimental details

The photocatalytic activities of the prepared samples were evaluated for Rhodamine B (RhB) degradation under visible light irradiation. In a typical photocatalysis experiment, 2.3 ml RhB (3.5 mg/L) aqueous solution and 0.1 mg photocatalyst were mixed in a standard 4 ml quartz cuvette. Subsequently, 6uL of 0.1M HCl was added to maintain the reaction mixture pH at 3. The reaction mixture was stirred (in the dark) for 20 minutes to achieve an adsorption-desorption equilibrium. Then this reaction mixture was placed under visible light irradiation in a homemade photocatalytic chamber under a 14W Philips cool white LED bulb (720 W/m^2 intensity)

visible light source. The absorption spectrum of the mixture was recorded at regular time intervals.

5.3 Results and discussion

5.3.1 Structural properties

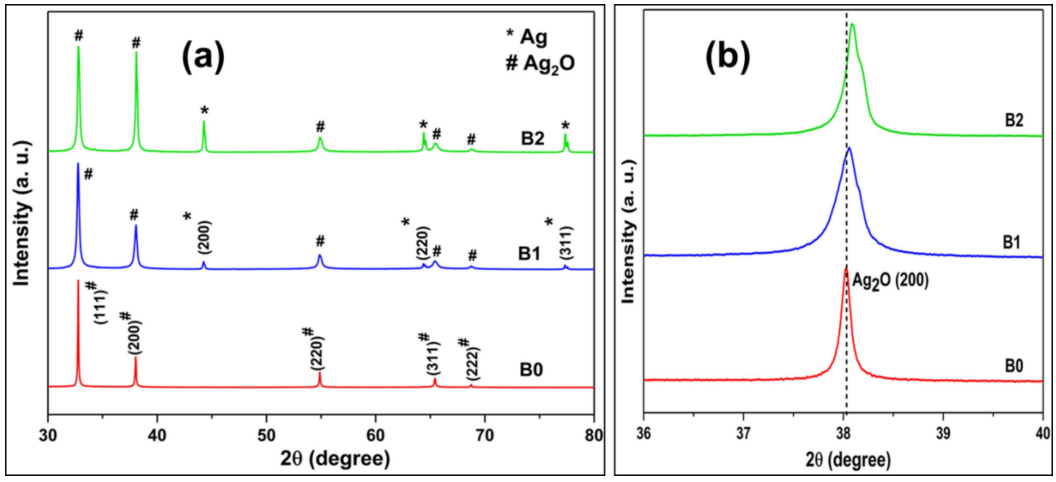

Figure 5.2 (a) Powder XRD patterns of the undoped and S-doped Ag_2O samples, (b) A comparison of the B0, B1, and B2 Ag_2O (200) plane XRD reflections (zoomed-in Ag_2O (200) peak).

Figure 5.2a displays the powder XRD patterns of undoped and S-doped Ag_2O nanoparticles. All peaks in the XRD of different samples match the standard FCC Ag_2O (JCPDS Card No. 75-1532) pattern. In addition, the doped samples (B1 and B2) also contain FCC Ag phases (JCPDS Card No. 89-3722). These XRD plots do not have any peak corresponding to Ag_2SO_4 or Ag_2SO_3 phases. Figure 5.3 shows the XRD pattern of the B3 sample with the highest S-doping (2.5 mol%) attempted. This XRD pattern has FCC Ag_2O, face-centered orthorhombic Ag_2SO_4 (JCPDS Card No. 80-1270), monoclinic primitive Ag_2SO_3 (JCPDS Card No. 70-1910), and orthorhombic Ag_2S phases. Since excess incorporation of sulfur causes phase separation into Ag_2SO_4, Ag_2SO_3, and Ag_2S phases (besides the parent Ag_2O structure), doping experiments with

higher dopant mole percentages were not attempted (De et al., 2020). Therefore, the B3 sample was not used for any photocatalytic performance evaluations.

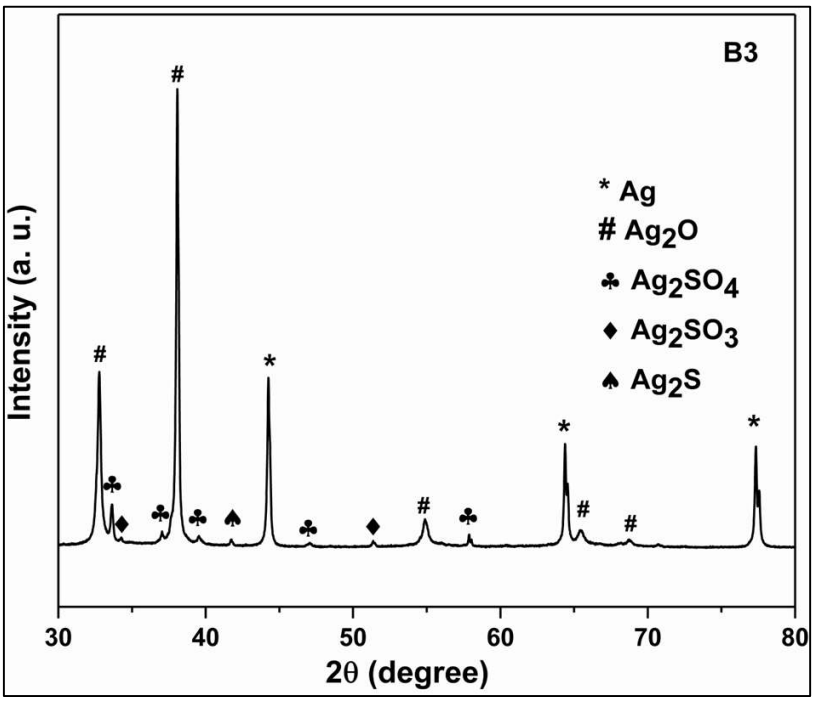

Figure 5.3 Powder XRD pattern of B3 sample.

Figure 5.2b compares the peak positions of the Ag_2O (200) plane for different samples. The diffraction peaks shift towards a higher Bragg's angle with an increasing dopant concentration. Thus, increased S-doping causes lattice contraction. The third column of Table 5.1 displays the lattice parameters of S0, S1, and S2 systems. Sulfur can exhibit -2, +4, and +6 oxidation states. But +4 and +6 oxidation states would entail the formation of Ag_2SO_3 and Ag_2SO_4 compounds/phases. Since these phases have not been formed, the reason for lattice contraction has to be different. One reason for the contraction of the Ag_2O lattice could be oxygen vacancies. This aspect is investigated in sub-sections 5.3.5 (XPS analysis) and 5.3.6 (DFT calculation results).

5.3.2 TEM and SEM analysis

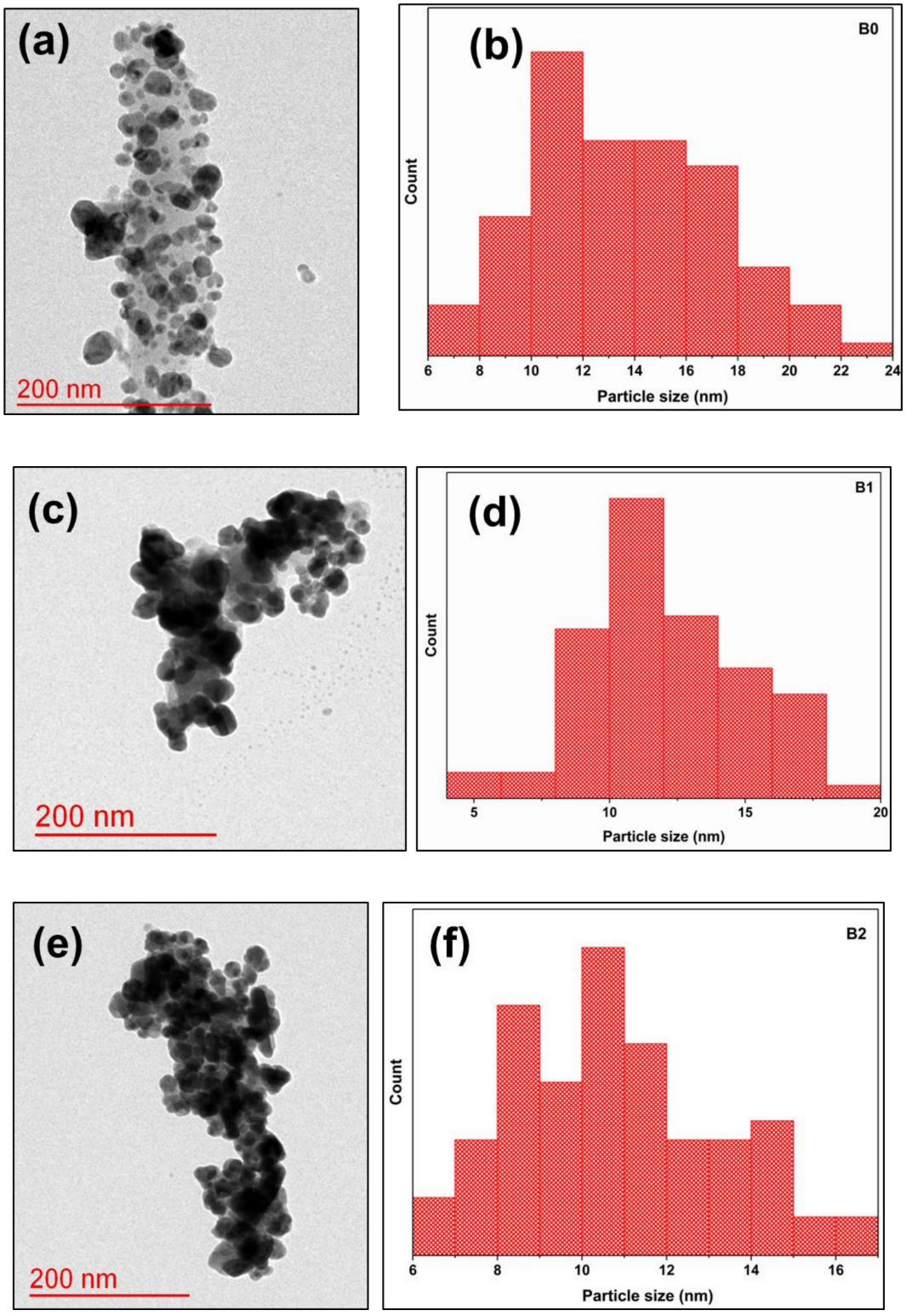

Figure 5.4 TEM images of B0 (a), B1 (c), B2 (e) and the particle size distribution of B0 (b), B1 (d), B2 (f).

TEM images give the shape and size of the prepared nanoparticles. Figure 5.4 displays the particle morphologies and size distributions of samples B0, B1, and B2, respectively. All synthesized nanoparticles are approximately spherical. Table 5.1 tabulates the synthesized nanoparticles' particle size and lattice parameter. Particle sizes decrease with the S doping. The incorporation of the dopant disrupts the regular symmetry of the pure crystal lattice (G. Xiang et al., 2015). Figure 5.5(a) and (b) display the high-resolution SEM images of B1 and B2 (doped samples). The respective elemental analysis tables are also attached with the corresponding images. This result indicates the presence of sulfur in all the doped samples.

Table 5.1 Variation in lattice parameter and average particle size with dopant concentration.

Dopant concentration (mole%)	Particle size (nm)	Lattice parameter (Å)
0	13.6	4.7292
0.3	12.1	4.7278
1.25	11	4.7214

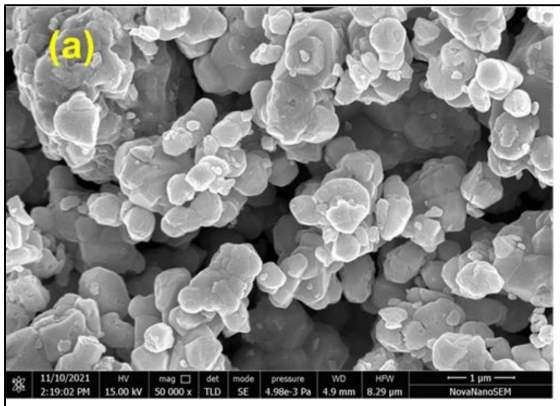

B1 sample		
Element	Weight %	Atomic %
O K	3.09	17.36
S K	0.95	2.67
AgL	95.96	79.97

B2 sample		
Element	Weight %	Atomic %
O K	2.48	14.23
S K	1.30	3.73
AgL	96.22	82.04

Figure 5.5 High-resolution SEM micrographs of (a) B1 and (b) B2 samples.

5.3.3 The bandgap

Figure 5.6a shows the solid-state UV-Vis absorption spectra of the samples prepared in this study. Equation (5.3) gives the Tauc relation for finding the bandgap of the as-prepared nanomaterials.

$$(\alpha h\nu)^{\frac{1}{n}} = h\nu - E_g \qquad (5.3)$$

The bandgap is denoted by E_g, α represents the absorbance, h is the Plank's constant, and ϑ is the frequency. When n = ½, the graph is for the indirect bandgap, and n = 2 represents the direct bandgap plot. The x-axis intercept of the linear fit to the constant slope region of this plot gives the material bandgap (depicted in Figure 5.6b). The

bandgaps of B0, B1, and B2 are 1.53, 1.70, and 1.89 eV, respectively. Thus, the bandgap increased with the dopant concentration.

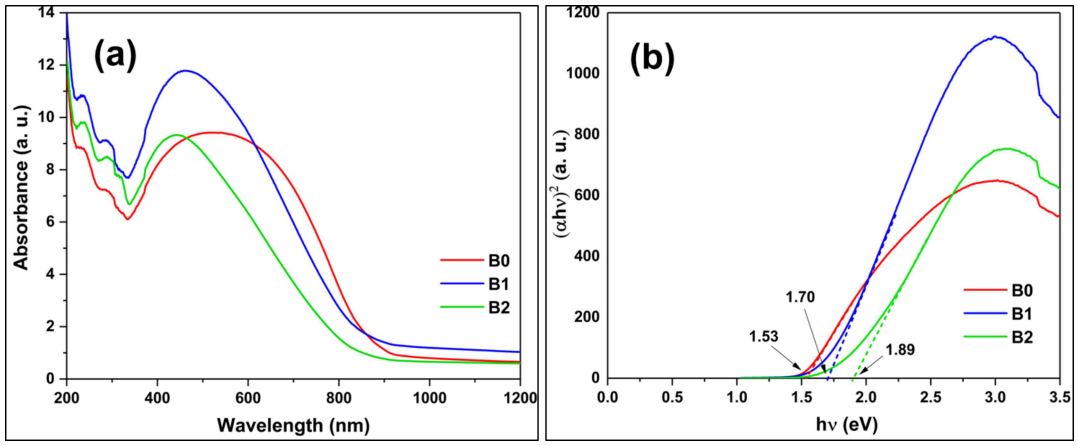

Figure 5.6 (a) The solid-state UV-visible absorption spectra and (b) Tauc plots of B0, B1, and B2 samples.

5.3.4 Photoluminescence studies

The emission (fluorescence) intensity can analyze the relative recombination efficiency. Lower intensity points to a slower recombination process and thereby improves charge separation. Figure 5.7 presents a comparison of PL spectra of doped nanomaterials with the undoped ones. The doped materials show lower intensity in comparison to the undoped analog. For the B2 sample, the intensity is the least. As reported in section 5.3.7, the B2 sample shows the maximum photocatalytic activity among the investigated samples.

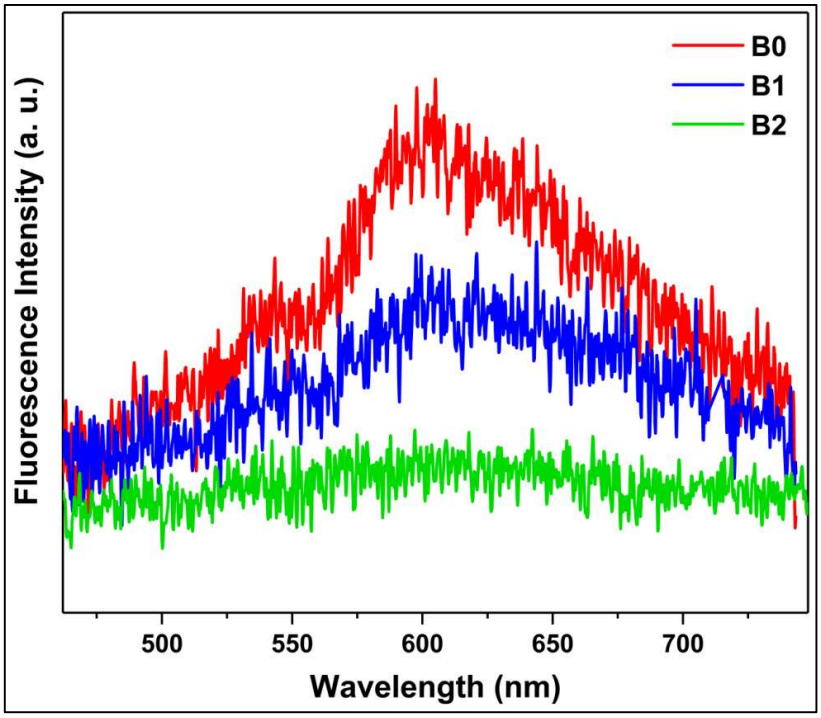

Figure 5.7 A comparison of the PL spectrum of B0, B1, and B2 samples.

5.3.5 XPS analysis

Figure 5.8 represent the survey XPS spectra of undoped (B0) and doped (B2) samples. The integration of the S2p peak area shows 0.97 atom percent of sulfur on the B2 surface. Furthermore, the O/Ag atomic concentration ratio is 0.476, less than 0.5.

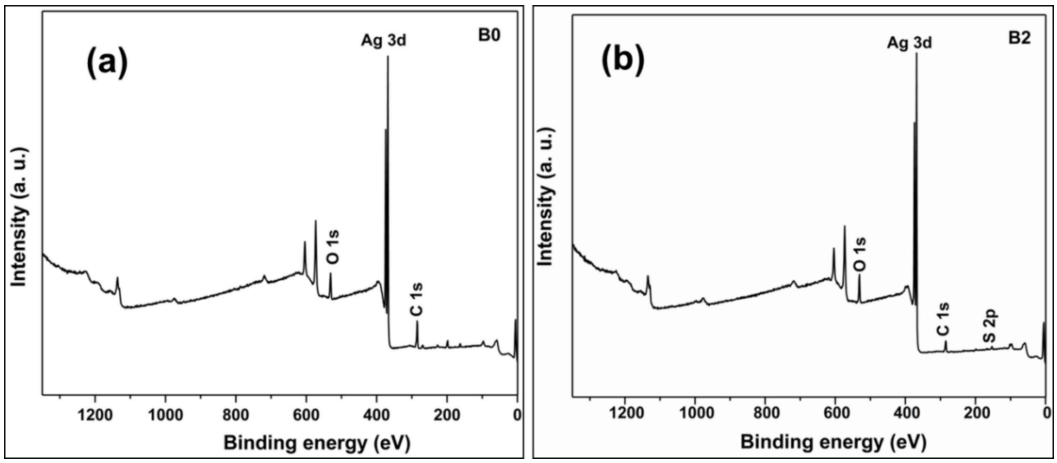

Figure 5.8 XPS survey spectrum of (a) B0 and (b) B2 samples.

The O1s spectrum was deconvoluted to estimate the various oxygen species in these nanomaterials. Figure 5.9 (a,b) displays the high-resolution O1s XPS spectra of the B0 and B2 samples. The deconvolution of O1s peak gives chemisorbed oxygen (O_C), lattice oxygen (O_L), and oxygen vacancy (O_V) regions. Different colors highlight these regions in the O1s curve. Both B0 and B2 O1s peaks showed significant areas under the O_V curves. But the B2 sample O_v curve area is substantially higher and thus implies more oxygen vacancies. Thus, S-doping increases the OV percentage. Note that the O_V region in the deconvoluted O1s peak represents oxygens neighboring the vacancies in the anion sub-lattice. These oxygens have coordination dissimilar to the perfect Ag_2O case (Gao et al., 2017). Sample B2 also exhibits significant Ag^0 formation (see XRD in Figure 5.2a). Oxygen vacancies leave excess electrons in the lattice, and these are used to form Ag^0. Furthermore, the B2 O_C percentage is substantially lesser than B0.

When sulfur goes into the Ag_2O lattice, it could be in +6, +4, or -2 oxidation states. The deconvolution of S 2p (shown in Figure 5.9c) high-resolution peak shows that sulfur in all three oxidation states is present in the B2 sample. Most sulfur is in the +6 oxidation state, while a relatively small part is in the -2 oxidation state. Figure 5.10 compares the Ag 3d XPS spectra of the B0 and B2 samples. Doping shifts the $3d_{5/2}$ and $3d_{3/2}$ peaks to lower binding energy values. It seems that S-doping causes charge transfer to the Ag part and decreases its binding energy.

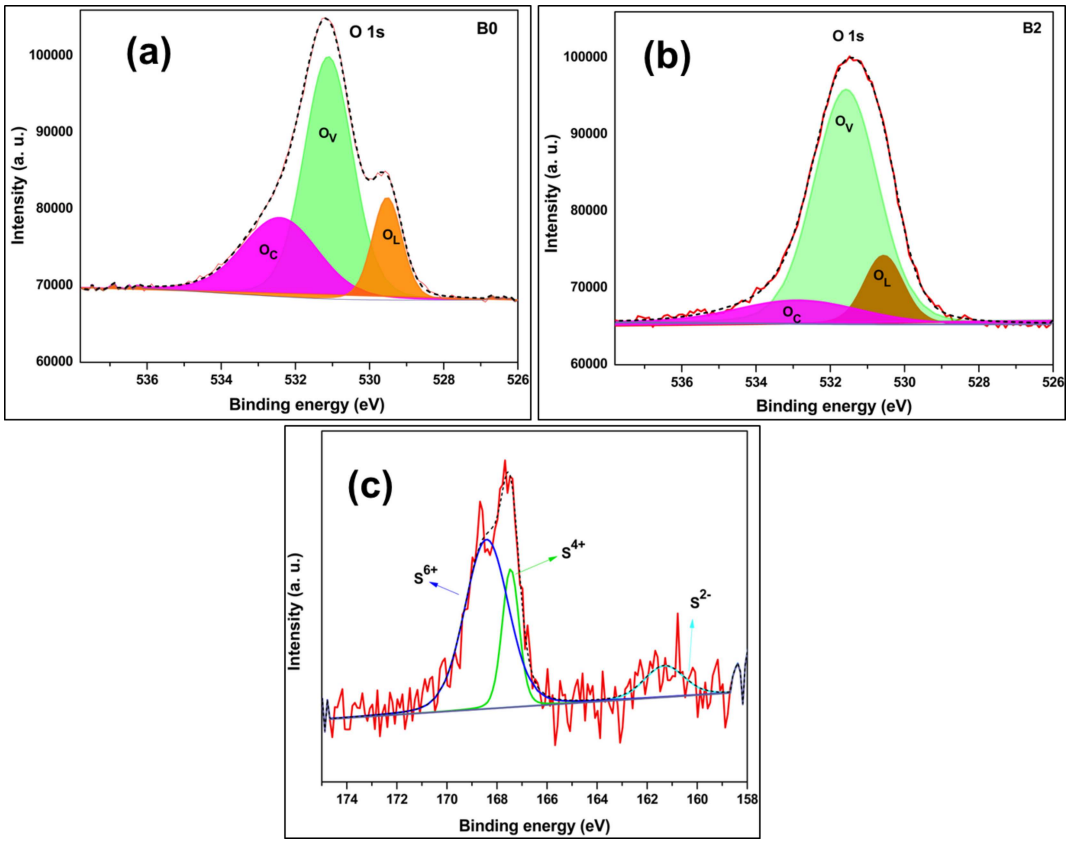

Figure 5.9 High resolution XPS spectrum of O 1s for (a) B0 and (b) B2 samples (c) high resolution XPS spectrum of S 2p for B2 sample.

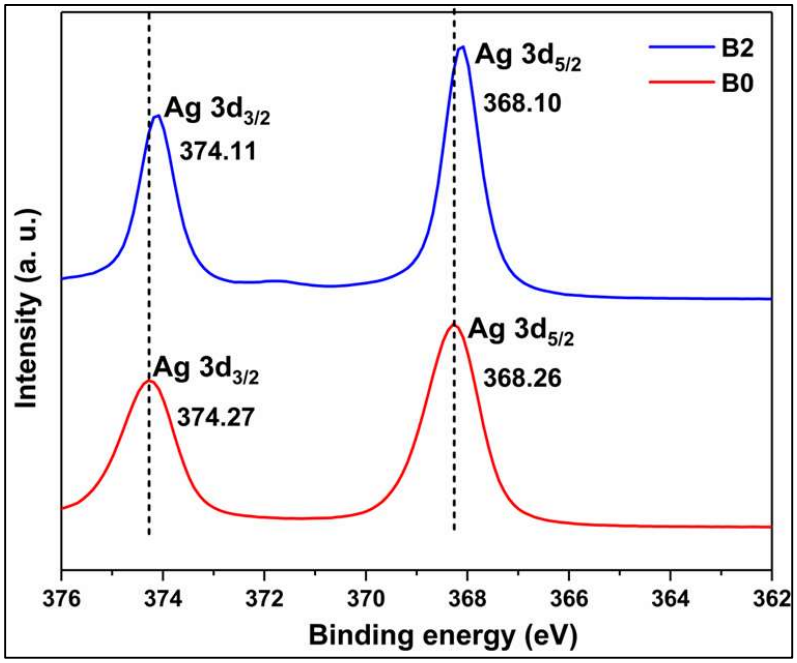

Figure 5.10 Comparison of high-resolution XPS spectrum of Ag 3d for undoped (B0) and doped (B2) Ag_2O.

Furthermore, the combination of UV-DRS and valence band XPS (in Figure 5.11) was used to obtain the VB and CB positions of the prepared nanoparticles. Table 5.2 displays the VB and CB positions (from VB-XPS) of the Ag_2O (doped and undoped) samples prepared in this study. The VB and CB positions of B2 are located at -0.46 and -2.35 eV. Compared to B0, sulfur-doped samples exhibit a significantly negative VB value.

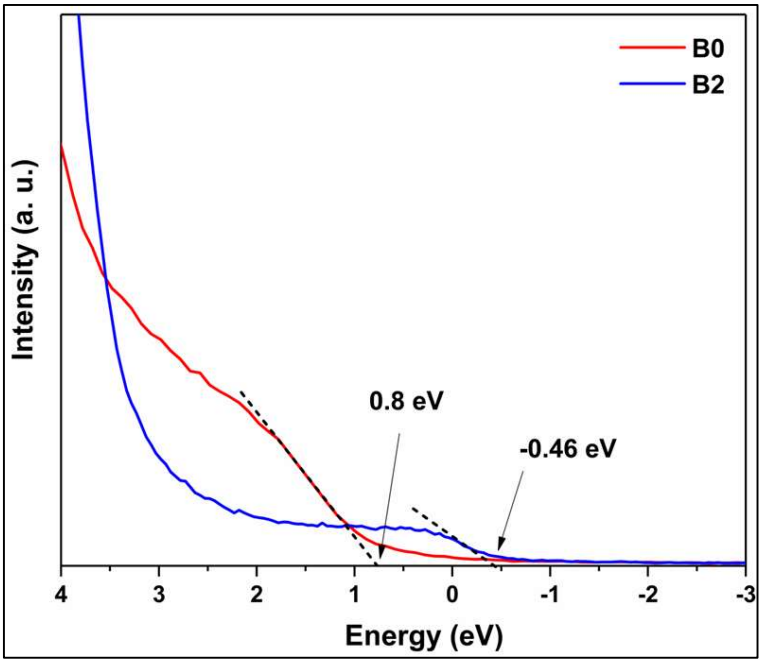

Figure 5.11 Valence band XPS spectrum of B0 and B2 samples.

Table 5.2 The position of VB and CB for the undoped and doped samples.

Samples	VB (eV)	CB (eV)
B0	0.80	-0.73
B1	-0.48	-2.18
B2	-0.46	-2.35

5.3.6 DFT calculation results

As mentioned earlier, the results of DFT calculations on different sulfur-doped models motivated the experimental investigations. The first calculations were on C0, CP1, and CP2 models. Table 5.3 describes the results of these calculations. The formation energy of a sulfur atom substituting oxygen (CP1) was lower than that found for CP2, indicating the former is favored thermodynamically.

Table 5.3 The formation energies and bandgap values of all the models attempted from DFT analysis.

Model	Formation energy (eV)	Bandgap (eV)
C0	-	0.00
CP1	0.71	0.06
CP2	1.97	0.0
C1	0.75	0.480
C2	0.63	0.54
C3	1.54	0.08
C4	1.81	0.518

It is crucial to note that the GGA-PBE functional used in the present investigation grossly underestimates the bandgap and gives a zero bandgap result for the pure Ag_2O model (De et al., 2020; Morales-García et al., 2017a). Sulfur substitution of oxygen (CP1) increased this bandgap (0.06 eV), qualitatively indicating that S-doping would increase the Ag_2O bandgap.

The next set of calculations attempted to elucidate the effect of oxygen vacancy on sulfur doping (or vice versa). Thus, S-doped OV-Ag_2O models (C2 and C3) are compared with the undoped OV-Ag_2O (C1) model. Table 5.3 summarizes the results of the DFT calculations on these systems. The calculated formation energy of the C2 and C3 models are 0.63 and 1.54 eV, respectively. Thus, substitutional doping (C2) is favored. The existence of sulfur in +4 or +6 oxidation states (from XPS) could be due to the formation of small Ag_2SO_3 and Ag_2SO_4 clusters. XRD would not detect these due to a lack of long-range order.

The substitutionally doped system (C2) also shows a larger bandgap (0.536 eV) than C1 (0.48 eV). Figure 5.12 gives the DFT calculated band structures of the C1 and C2 models, showing the bandgap. But, substitutional or interstitial S-doping causes

lattice expansion in contrast to experimental (XRD) observation. Since S-doping also increases OVs, therefore DFT calculations were also conducted on another model with two only OVs (no S-doping). We denote this model by C4. Enhanced OVs contract the Ag_2O lattice (see Table 5.4). Furthermore, it also increases the bandgap (see Table 5.3).

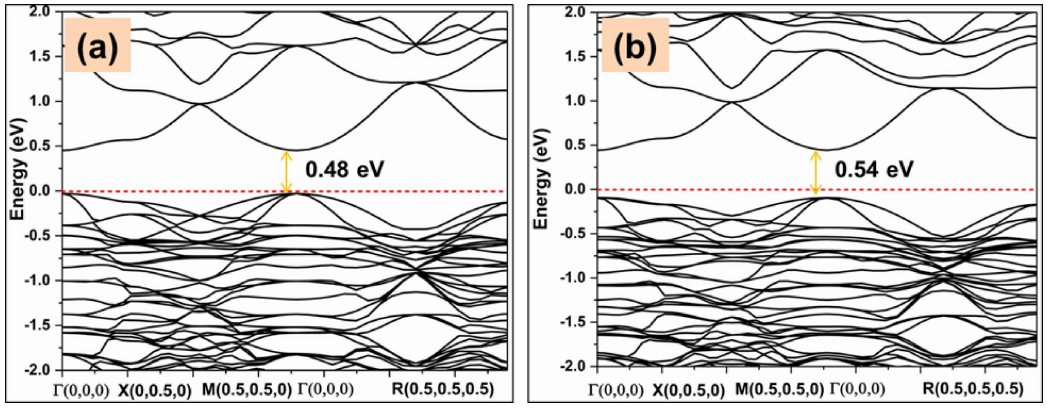

Figure 5.12 Band structure of (a) OV Ag_2O (C1 model), (b) OV Ag_2O with substitutional S doping (C2 model).

Table 5.4 Change of the lattice parameters on the increment of OV in Ag_2O lattice.

Lattice parameters	Without OV	1OV (C1)	2OV (C4)
A	9.63	9.53	9.46
B	9.63	9.53	9.45
C	9.63	9.53	9.46
α	90	90	90
β	90	90	90
γ	90	90	90
Volume	894.11	866.38	844.94

Figure 5.13 compares the TDOS of OV Ag_2O with the S-doped Ag_2O. The inset figure shows that the doped system states near the Fermi region shifted to the higher energy region. Note that the Fermi level is set at zero energy on the x-axis.

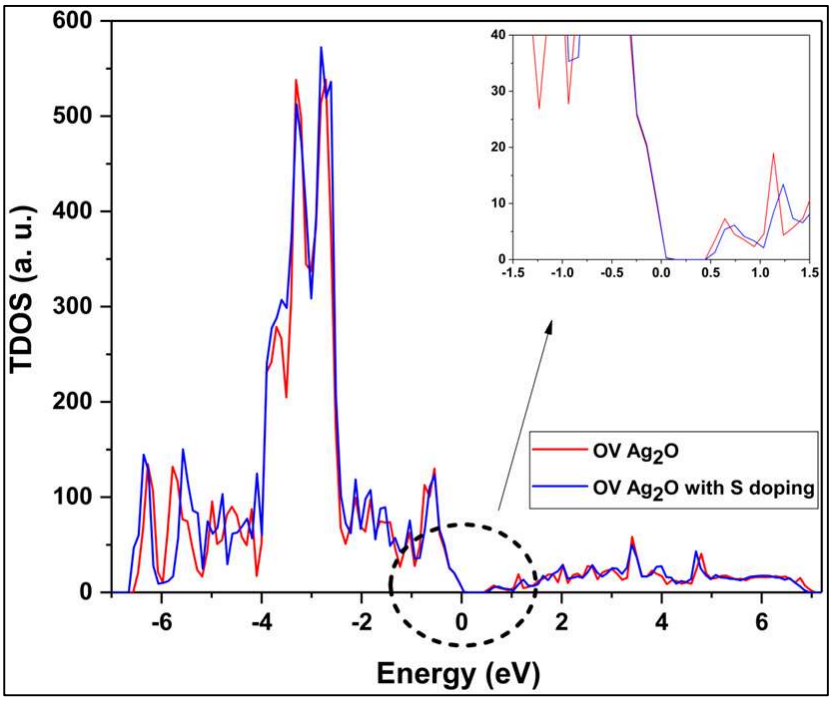

Figure 5.13 Comparison of TDOS of OV Ag_2O (C1 model) and S doped Ag_2O system (C2 model).

Given the lowest formation energy of C2, Figure 5.14 displays the total density of states (TDOS) and partial density of states (PDOS) of the respective atomic orbitals of the C2 model system. The VB and CB refer to the diagram's negative and positive energy regions. The O 2p and Ag 4d orbitals mainly contribute to the VB electron density.

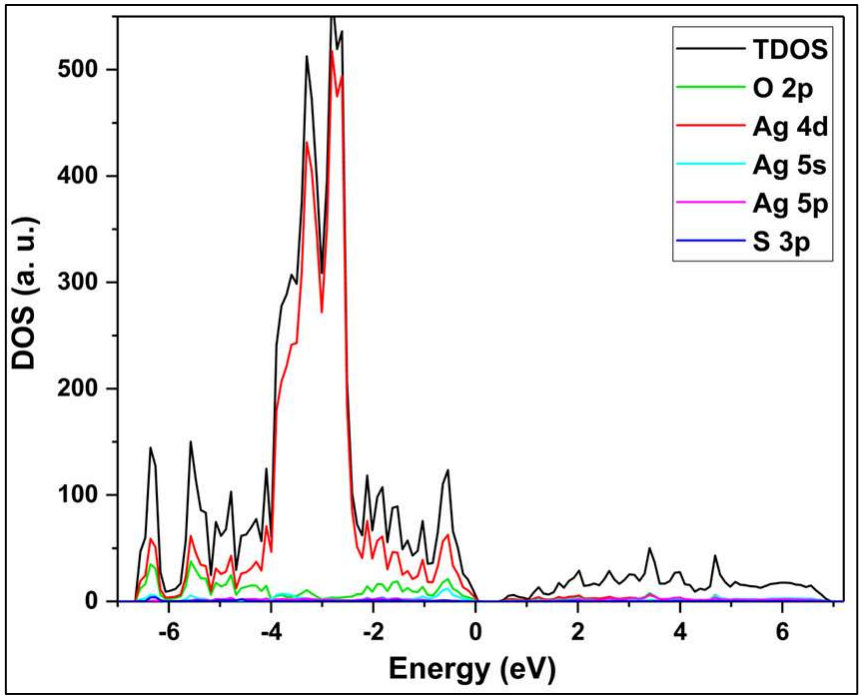

Figure 5.14 The TDOS and PDOS for OV Ag_2O with substitutional S doping system (C2 model).

On the other hand, the CB electron densities are primarily due to the Ag 5s and Ag 5p orbital. On S-doping, there is a considerable amount of hybridization between the atomic orbitals of Ag_2O (O 2p, Ag 4d, Ag 5s, Ag 5p) and dopant's atomic orbitals (S 3s, S 3p, and S 3d). As shown in Figure 5.15, the PDOS of S 3p is higher than those of S 3s and S 3d states and seems to be the main contributor to the electronic structure changes in S-doped Ag_2O.

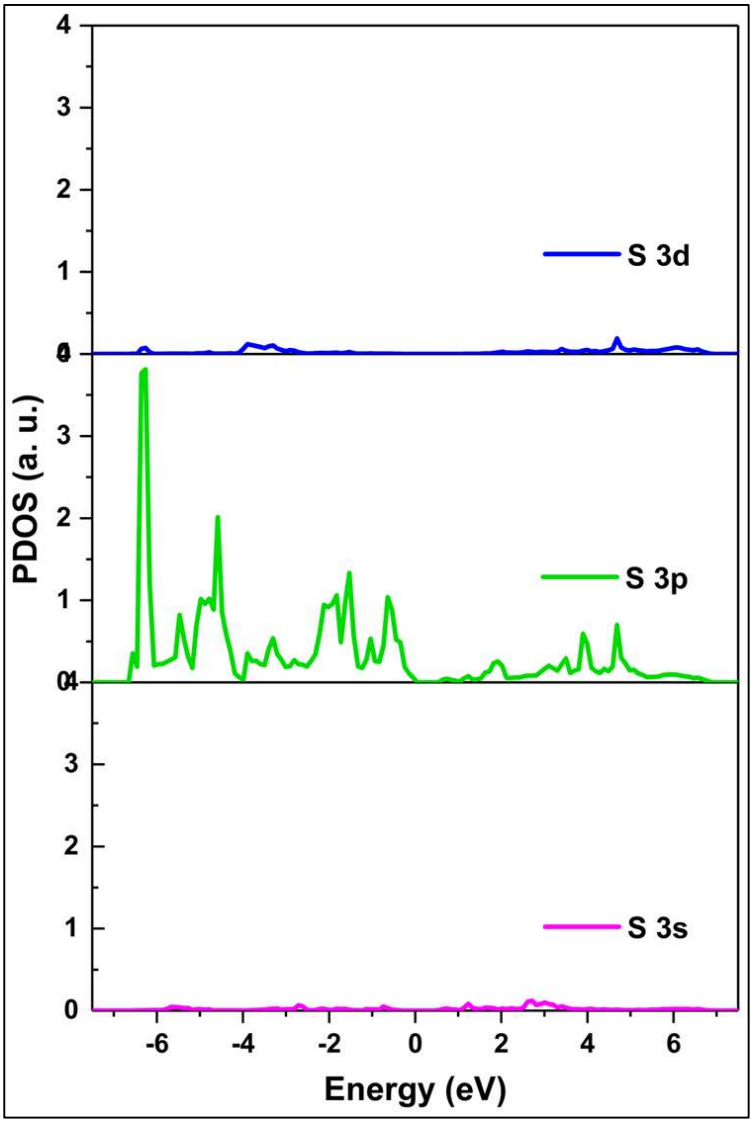

Figure 5.15 Comparison of PDOS of the dopant's atomic orbitals.

5.3.7 Photocatalytic properties

The visible photocatalytic activities of the as-prepared nanomaterials are tested for RhB degradation. Figure 5.16a shows the photocatalytic activities of the synthesized materials. RhB degrades at a higher rate on B1 and B2 than B0. But B2 exhibits the best RhB degradation activity.

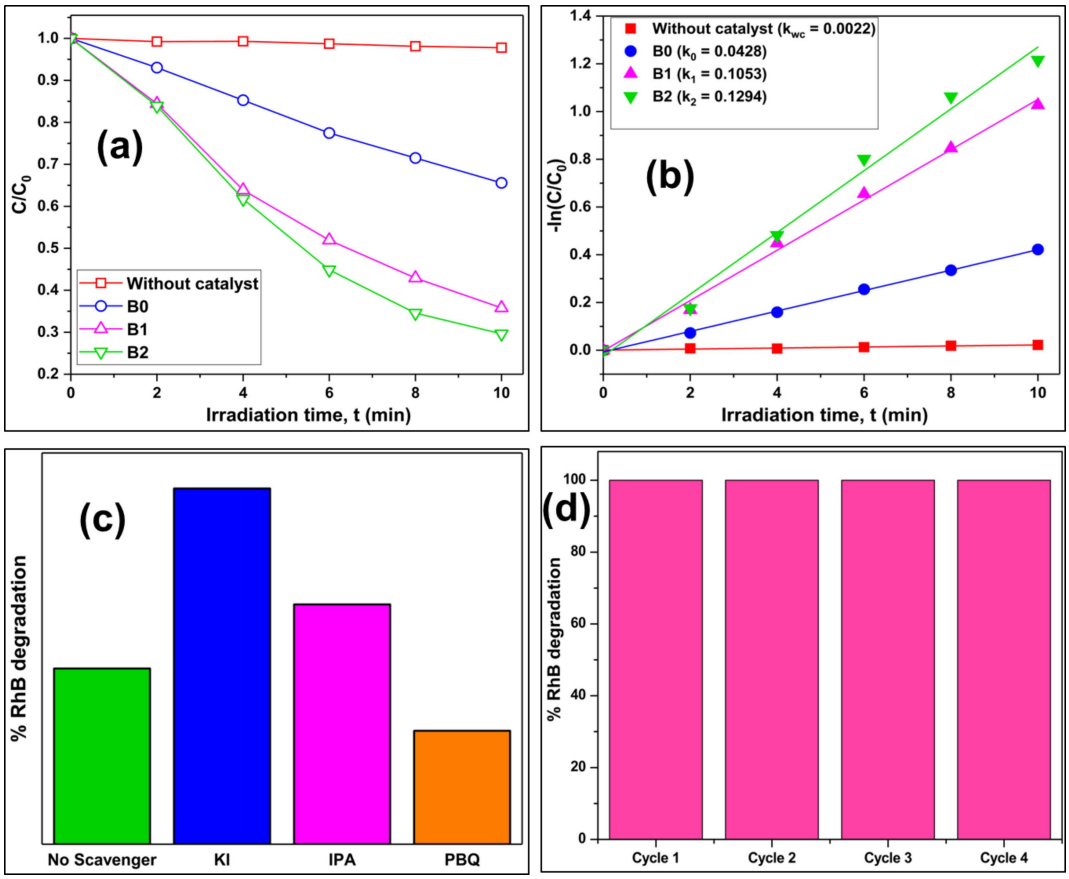

Figure 5.16 (a) Plots of RhB degradation with irradiation time, (b) kinetics plots – $\ln(C/C_0)$ vs. t over different photocatalysts, (c) results of scavenging experiments with on the B2 photocatalyst catalyst, and (d) recyclability tests of the B2 photocatalyst.

Figure 5.17(a) and (b) display the time variation of UV-visible absorption spectra of an aqueous solution of RhB over B0 and B2 photocatalysts. The B0 catalyst gives complete RhB degradation in 185 minutes. But RhB degradation over the B2 photocatalyst takes 35 minutes only.

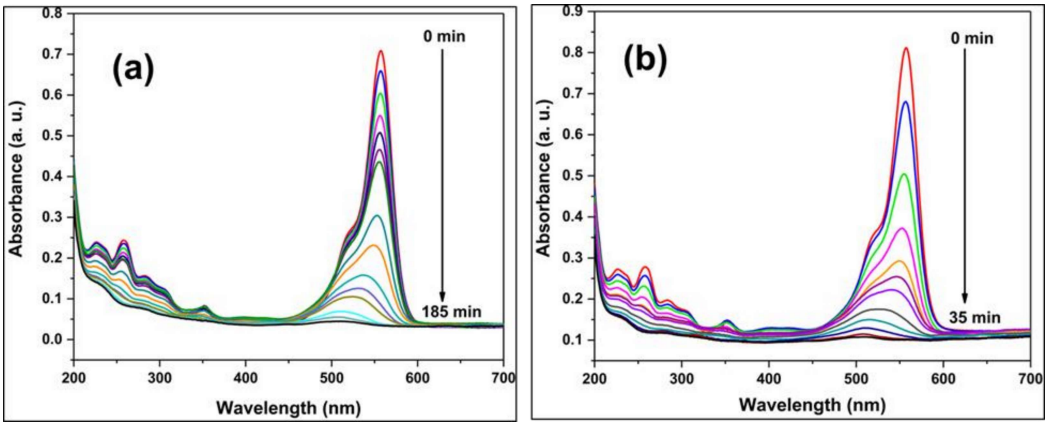

Figure 5.17 UV-Vis absorbance plot of RhB degradation on (a) B0 and (b) B2 photocatalysts.

There is no such degradation in the absence of a photocatalyst. RhB degradation over these photocatalysts follows pseudo-first-order kinetics (Eq. 5.4).

$$-\ln(C/C_0) = k_{app}t \qquad (5.4)$$

Here, C_0 is the initial concentration of the RhB aqueous solution, C is the concentration of the same after time *t*, and k_{app} is the apparent rate constant calculated from the slope of the linear fit to these plots. The kinetics plot is given in Figure 5.16b. The apparent rate constants were 0.0428, 0.1053, and 0.1294 min^{-1} for B0, B1, and B2 photocatalysts. The B2 photocatalyst shows the best catalytic activity on RhB degradation. Table 5.5 tabulates the turnover frequency (TOF) and apparent rate constant values for investigated photocatalysts.

The scavenging experiments were also performed to evaluate the reactive species during photocatalysis over the B2 sample (Figure 5.16c). Separate photocatalysis experiments were conducted with potassium iodide (KI), isopropyl alcohol (IPA), and p-benzoquinone (PBQ) for scavenging holes (h^+), hydroxyl radicals ($^{\cdot}$ OH), and superoxide radicals ($O_2^{\cdot-}$), respectively. The addition of KI and IPA

increased the RhB degradation rate compared to without any scavenger. In contrast, the addition of PBQ significantly reduces the RhB degradation rate. Therefore, the $O_2^{-\cdot}$ is the main active species during the RhB photodegradation. Figure 5.16d shows the result of the reusability experiment of the B2 photocatalyst. The photocatalyst exhibits very good recyclability up to four cycles.

Table 5.5 Turn over frequency (TOF) and rate constant of B0, B1, and B2 catalysts for the photo-degradation of RhB.

Catalysts	TOF (mole $g^{-1}min^{-1}$)	Rate constant (k_{app}) (min^{-1})
B0	4.79×10^{-6}	0.0428
B1	9.75×10^{-6}	0.1053
B2	1.18×10^{-5}	0.1294

5.3.8 Plausible photocatalytic mechanism

Figure 5.18 gives a schematic presentation of RhB photodegradation on the B2 photocatalyst. Visible light irradiation excited the electrons (e^-) on the VB to the CB. Oxygen vacancies and S-doping defects trapped the photo-excited species to reduce recombination probabilities. Further, it is well known that a small amount of Ag with Ag_2O helps to enhance the photocatalytic performance, increasing charge separation in the material. Metallic Ag can exhibit surface plasmon resonance (SPR) during light irradiation to enhance the photo efficiency and the charge carrier separation (Xuefei Wang et al., 2011; H. Xu et al., 2018). Light irradiation also led to photo-excitation of the RhB dye since its HOMO-LUMO gap is in the visible range. The photo-excited

electrons were transferred from the LUMO of the dye to quench the holes on the photocatalyst VB. At the same time, the highly negative CB position led to superoxide formation, which in turn degraded RhB. But, photo-excited holes are quenched better by KI and IPA, increasing the photocatalytic kinetics compared to the situation with no scavenger molecule. The RhB molecule interaction with the photocatalyst surface seems weaker than that with KI and IPA.

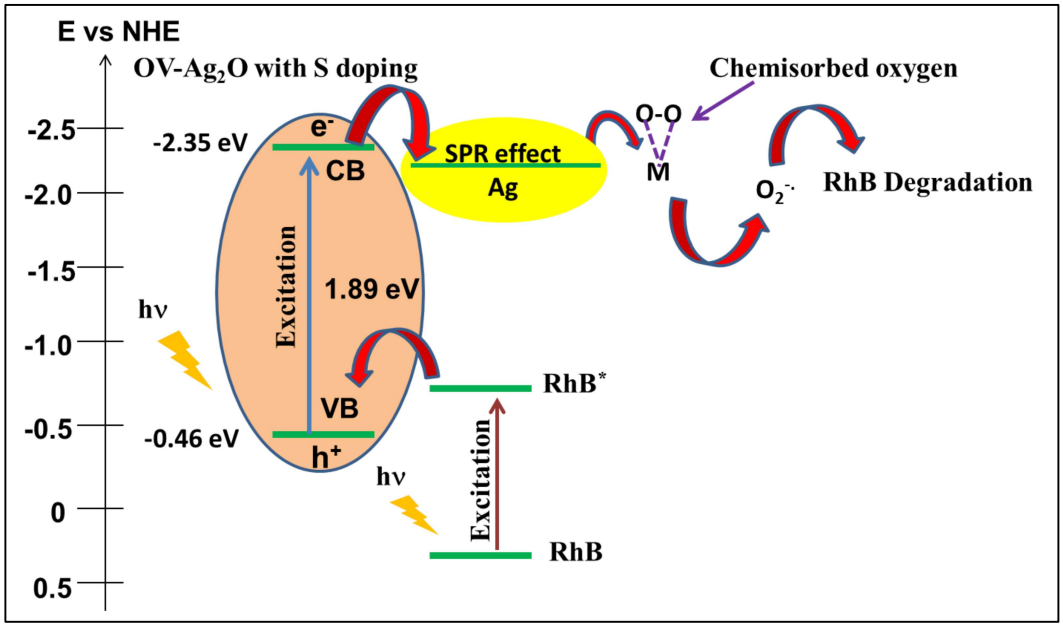

Figure 5.18 Possible RhB degradation photocatalytic mechanism.

S doping causes a shift of CB from -0.73 (B0) to -2.35 eV (B2). It also increases the OV proportion compared to the pure one. Further, these defects can also increase the charge separation in the doped systems. Therefore, higher CB potential and OVs in the doped Ag_2O facilities faster superoxide radicals formation, mainly responsible for the enhanced degradation efficiency in the doped samples.

5.4 Conclusions

Motivated by initial DFT predictions, sulfur-doped Ag_2O nanoparticles were prepared by a hydrothermal precipitation protocol. Sulfur doping could be achieved only up to 1.25%. Doping beyond this percentage led to the formation of multiple compound phases (Ag_2SO_3, Ag_2SO_4, etc.). Sulfur-doping up to 1.25% increased the bandgap substantially to 1.89 eV. DFT calculations predicted that substituting oxygen with sulfur could widen the Ag_2O bandgap and stabilize oxygen vacancies.

Furthermore, increased oxygen vacancies contracted the doped-Ag_2O lattice. XPS analysis also showed that sulfur-doping increases oxygen vacancies. Photoluminescence investigations showed that recombination probability decreased with doping. The photocatalytic activity of the Ag_2O nanoparticles towards rhodamine B degradation increased with sulfur doping. The substantial change in the electronic structure of Ag_2O nanoparticles due to oxygen vacancy and sulfur doping implies that these are virtually new photocatalysts.